RESEARCH ARTICLE

NANO · MICRO small
www.small-journal.com

Mechanistic Insights into Performance and Stability Enhancement of Infiltrated Solid Oxide Electrochemical Cell Electrodes

Jinsil Lee, Jinhong Park, Taeyun Kim, Soomin Choi, Seong Kyun Kim, Kyung Joong Yoon, and Jong Hoon Joo**

Surface modification via nanocatalyst infiltration has emerged as an effective strategy for enhancing the performance and lifespan of high-temperature electrochemical devices, addressing the limitations of conventional perovskite-based air electrodes. Although surface modification has been widely adopted, how infiltration simultaneously enhances electrochemical activity and durability remains unclear. Herein, the effect of $Sm_{0.5}Sr_{0.5}CoO_{3-\delta}$ (SSC) infiltration into $La_{0.6}Sr_{0.4}Co_{0.2}Fe_{0.8}O_{3-\delta}$ (LSCF) electrodes is systematically investigated using dense model systems, which enable for detailed analysis of surface phenomena and accurate quantification of electrochemical processes. The SSC coating significantly enhanced the oxygen surface-exchange kinetics while concurrently suppressing cation segregation and phase decomposition under the solid oxide fuel cell (SOFC) operating conditions. This improvement is attributed to the reduced electrode polarization via the catalytic promotion of surface reactions, which lowers the surface potential and mitigates instability in the LSCF backbone. These findings are consistently validated in full-cell configurations, confirming that infiltration not only improved performance but also suppressed Cr poisoning and phase decomposition. This study offers new insights into the dual role of infiltration in enhancing both the catalytic activity and structural stability, establishing design principles for durable, high-performance SOFC electrodes.

1. Introduction

The demand for efficient, durable, and sustainable energy-conversion technologies is growing rapidly as the world transitions toward decarbonized energy systems. Among them, high-temperature electrochemical devices, such as solid oxide electrolyzer cell (SOEC) and solid oxide fuel cell (SOFC), offer unique advantages, including high conversion efficiency, fuel flexibility, and compatibility with renewable energy sources.[1–10] However, their long-term stability and performance under harsh operating conditions remain major bottlenecks for broad commercialization.[1–5,8,10–14] In particular, electrode degradation and sluggish surface reactions critically hinder the operational efficiency and durability of these systems. To address these issues, surface modification of electrodes has emerged as a promising strategy for enhancing interfacial activity, promoting reaction kinetics, and suppressing degradation.[4–6] Through approaches such as nanocatalyst coating, heterointerface engineering, or functional layer deposition, surface-modified electrodes can offer improved catalytic performance while maintaining structural and chemical stability. These techniques enable the incorporation of high-activity materials that may be incompatible with conventional high-temperature fabrication routes. The need for improved interfacial reactivity is particularly pronounced in solid oxide electrochemical cells, where the oxygen-exchange reaction at the air electrode is

J. Lee, T. Kim, S. Choi, S. K. Kim, J. H. Joo
Department of Environment and Energy Engineering
Gwangju Institute of Science and Technology
123, Cheomdangwagi-ro, Buk-gu, Gwangju 61005, Republic of Korea
E-mail: jhjoo@gist.ac.kr

The ORCID identification number(s) for the author(s) of this article can be found under https://doi.org/10.1002/smll.202506595

DOI: 10.1002/smll.202506595

J. Park, K. J. Yoon
Center for Energy Materials Research
Korea Institute of Science and Technology (KIST)
Seoul 02792, Republic of Korea
E-mail: kjyoon@kist.re.kr

J. Lee, S. K. Kim, J. H. Joo
Research Center for Innovative Energy and Carbon Optimized Synthesis for Chemicals (Inn-ECOSysChem)
Gwangju Institute of Science and Technology
123 Cheomdangwagi-ro, Buk-gu, Gwangju 61005, Republic of Korea

inherently sluggish and contributes significantly to performance losses.[4–6] Extensive efforts have been devoted to enhancing the catalytic activity and stability of air electrodes through surface-modification strategies. Among these surface-modification techniques, the infiltration method has drawn interest for its ability to introduce highly active nanocatalyst layers into the porous backbone electrode, thereby significantly enhancing the electrochemical activity.[7–13] This approach accommodates a wide variety of active materials that may otherwise be incompatible with conventional high-temperature fabrication processes owing to reactivity or cost constraints.[10,11] Furthermore, it enhances performance by reinforcing interface adhesion and increasing the number of active reaction sites, thereby ensuring substantial performance improvements.[10,12,15] To date, a diverse range of materials, including perovskite oxides, such as $Sm_{0.5}Sr_{0.5}CoO_{3-\delta}$,[8–13,16–20] and fluorite oxides, such as $Ce_{0.8}Gd_{0.2}O_{2-\delta}$,[9,20–26] have been employed as infiltration materials. Extensive research has confirmed their effectiveness in enhancing both electrochemical performance and long-term operational stability.[8–13,17–27] Previous studies have reported that the composition, structure, and morphology of the infiltrated catalyst play a crucial role in enhancing performance.[8–13,17–27] Despite extensive research on infiltration, the interaction between infiltrated catalysts and the backbone remains highly complex due to several interrelated factors, including chemical reactions, elemental interdiffusion, and the formation of unfavorable secondary phases at the interface, and a clear understanding of the underlying reaction mechanisms is still lacking.[10] Moreover, although numerous studies have demonstrated that infiltration can lead to improvements in both electrochemical performance and long-term stability, the fundamental reasons behind this dual enhancement remain elusive. In particular, performance enhancement and long-term stability improvement are typically regarded as having a tradeoff relationship; however, the scientific principles governing their simultaneous enhancement remain poorly understood. Previous studies have primarily attributed the performance improvement of infiltrated electrodes to an increase in the number of reaction sites,[9–13,16–19,25,28] whereas the enhanced stability has often been simplistically explained by the suppression of nanoparticle coarsening and agglomeration.[9,11,12,16,17,20,24–26,28] However, such interpretations are insufficient to fully capture the complex electrochemical behavior of infiltrated electrodes. Therefore, more systematic and in-depth studies are required to elucidate the principles governing the improved electrochemical performance and long-term durability induced by infiltration.

Here, to eliminate the structural influence of highly porous backbone electrodes and shed light on the intrinsic characteristics of electrode reactions, $La_{0.6}Sr_{0.4}Co_{0.2}Fe_{0.8}O_{3-\delta}$ (LSCF), one of the most widely used air electrode materials in SOFC, was used to fabricate dense electrodes as model electrodes.[27,29–31] Subsequently, the highly active catalyst $Sm_{0.5}Sr_{0.5}CoO_{3-\delta}$ (SSC) was deposited into the surface of the dense LSCF electrode. Here, to eliminate the structural influence of highly porous backbone electrodes and shed light on the intrinsic characteristics of electrode reactions, $La_{0.6}Sr_{0.4}Co_{0.2}Fe_{0.8}O_{3-\delta}$ (LSCF) was employed to fabricate dense model electrodes.[27,29–31] LSCF is a representative perovskite-type oxide widely used in SOFC air electrodes due to its high mixed ionic and electronic conductivity and favorable catalytic activity. However, its relatively low surface exchange activity and limited long-term stability remain critical challenges.[10,32,33] To overcome these limitations, $Sm_{0.5}Sr_{0.5}CoO_{3-\delta}$ (SSC), which exhibits high oxygen-exchange kinetics and good chemical compatibility with LSCF, was infiltrated into the surface of the dense LSCF electrode to enhance surface functionality while retaining the intrinsic advantages of the backbone material. This approach minimizes the geometric effects of the electrode, providing a suitable platform for detailed surface-exchange reaction analysis, thereby enabling a more precise and quantitative investigation of the stability mechanisms associated with catalyst infiltration.[4–6,34,35] Furthermore, the platform utilizing a dense electrode allows for a more accurate assessment of the potential distribution across different electrochemical processes, facilitating a deeper understanding of electrode's performance enhancement and degradation mechanisms.[4–6,34,35] To validate the findings obtained from the model electrode, an actual SOFC cell was also analyzed. The cell was connected to a metallic interconnector, not only to facilitate the evaluation of degradation phenomena, but more importantly, to replicate the realistic operating conditions of SOFC systems, in which metallic interconnectors are integral components. The findings demonstrated that the LSCF cell infiltrated with SSC exhibited superior performance and stability compared with the non-infiltrated cell, which is consistent with the results from the dense bulk model electrode. This improvement can be attributed to the enhanced surface-exchange reaction facilitated by SSC infiltration, which concurrently reduces the surface potential of the LSCF, thereby significantly improving the phase stability by mitigating the formation of secondary phases and phase decomposition. Finally, this study reveals the critical role of infiltrated catalysts in enhancing the durability of SOFC by effectively mitigating degradation of the backbone electrodes.

2. Results and Discussion

2.1. Construction and Electrochemical Characterization of Dense Bulk Electrodes

Figure 1 schematically illustrates the SSC surface coating on a dense LSCF bulk electrode. First, the dense LSCF electrode was fabricated by co-sintering the GDC electrolyte and the LSCF electrode using the tape-casting method. This procedure has already been described in our previous research.[4,6] The use of a dense LSCF electrode eliminates the effects of microstructural variations induced by porous electrodes, thereby enabling precise analysis of surface-exchange reactions. Afterward, the fabricated LSCF dense bulk electrode was annealed at 450 °C for 5 min to remove unexpected impurities on the surface. Subsequently, 2.5 µL of SSC solution (0.5 M), prepared using a urea- and glycine-based infiltration technique, was deposited onto the LSCF surface, followed by annealing at 650 °C in air. This technique enabled the synthesis of a phase-pure SSC perovskite with a controlled morphology, as detailed in our previous studies.[9,11] To verify the successful formation of SSC on the LSCF electrode, SEM was used to analyze the dense electrode before infiltration, and SEM and EDX were used to analyze the electrode after infiltration (Figure 1b). As can be seen in Figure 1b, the LSCF surface was densely sintered, with an average grain size of 0.97 µm. Cross-sectional SEM analysis after infiltration confirmed that the SSC catalyst uniformly

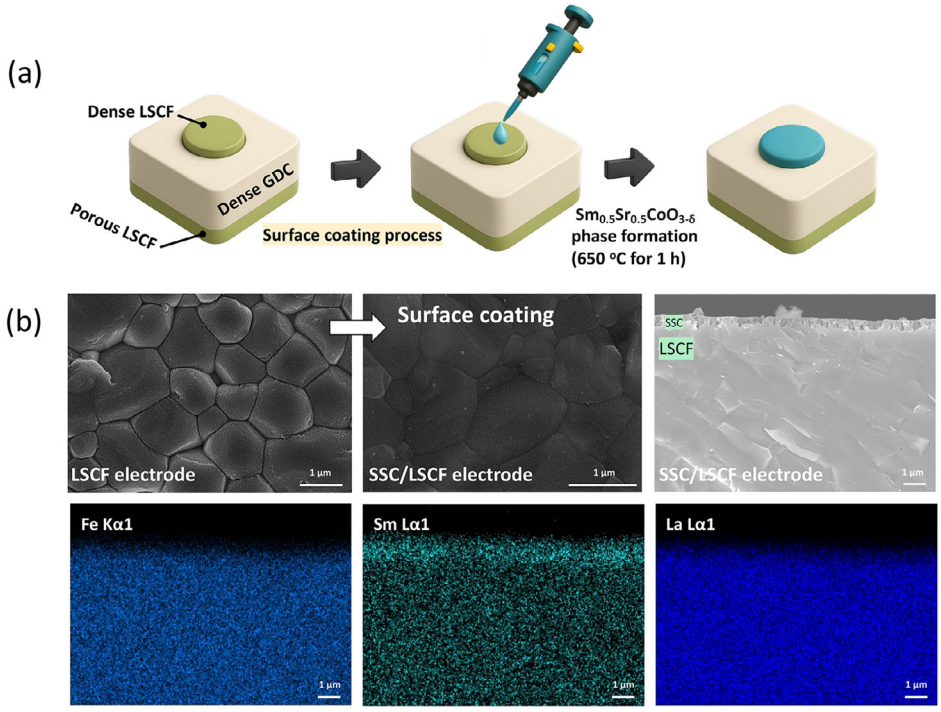

Figure 1. Overall process of infiltration strategy: a) schematic of the process of SSC surface coating onto the LSCF dense bulk electrode using the surface coating process, and b) SEM images of the LSCF electrode and SSC/LSCF electrode and EDX images of the SSC/LSCF electrode.

covered the LSCF grains, forming a continuous layer with an average thickness of several hundred nanometers. Also, EDX analysis was conducted to confirm the formation of the SSC phase, and the cross-mapping images of La $L\alpha_1$, Sm $L\alpha_1$, and Fe $K\alpha_1$ are shown in Figure 1b. Among the constituents of SSC and LSCF, Sm can serve as an indicator of the presence and uniformity of the SSC surface coating. The distribution of Sm across the entire surface indicates that the SSC layer was well-formed on top of the LSCF electrode. To investigate the influence of the SSC catalyst on the electrode reaction, the SSC/LSCF electrode was analyzed using impedance spectroscopy within the temperature range of 600–800 °C and then compared with the surface oxygen coefficient of LSCF and SSC materials. **Figure 2**a shows the representative impedance spectra of the LSCF and SSC/LSCF electrodes obtained under open-circuit voltage (OCV) at 700 °C. The simplicity of a dense electrode system allows its electrochemical properties to be clearly defined and understood through equivalent circuit representation. The characteristic thickness ($L_c = D/k$) is the

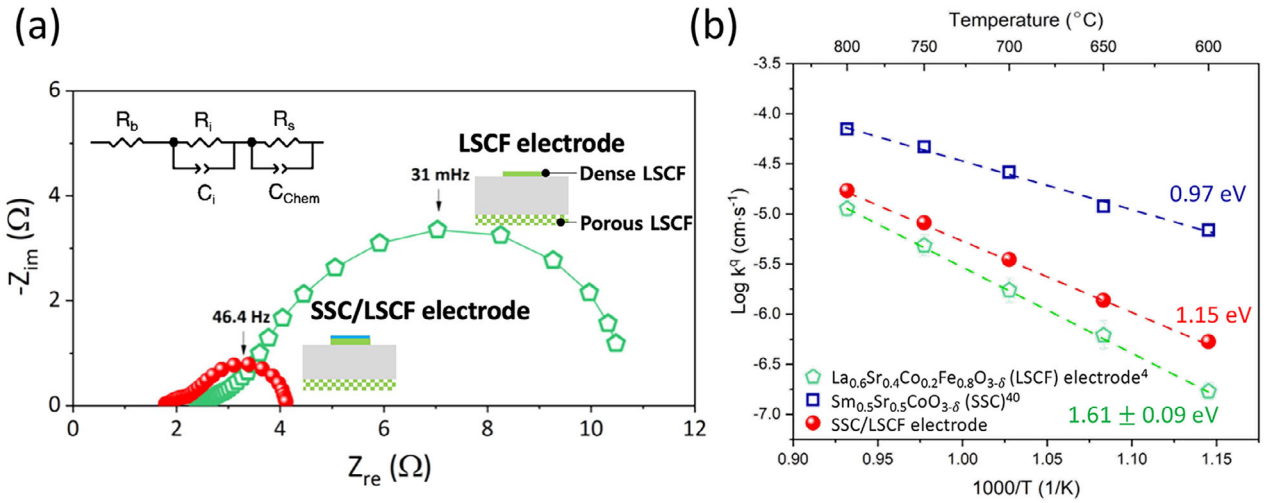

Figure 2. Electrochemical characterization of SSC/LSCF electrode. a) Impedance spectra of SSC/LSCF electrode at 700 °C. b) Arrhenius plots of surface-exchange coefficients of SSC/LSCF electrode and SSC, LSCF materials. The data were extracted from the tracer surface exchange coefficient (k^*) in ref. [40].

ratio of the bulk diffusion coefficient (D) to the surface-exchange coefficient (k). Since this dense electrode has a thickness of ≈15 µm, which is much smaller than the L_c of LSCF (typically a few hundred micrometers).[4,36] Therefore, bulk diffusion can be neglected in this electrode, and only the surface-exchange reaction needs to be considered.

The impedance pattern was analyzed using the equivalent circuit shown in Figure 2a. The impedance spectrum is characterized by three distinguishable components: the x-axis intercept at high frequencies, a semicircle at medium frequencies, and the largest semicircle at low frequencies. In our previous studies, we demonstrated that the three components in the equivalent circuit are the GDC electrolyte resistance (R_b), resistance of the electrode/electrolyte interface (R_i), and oxygen surface-exchange resistance (R_s).[4,6] When comparing the impedance patterns before and after SSC deposition, it was observed that while the changes in R_b, R_i were negligible, there was a noticeable decrease in R_s. This is attributed to the higher ionic conductivity and surface-exchange kinetics of SSC compared to those of LSCF, which facilitate the surface-exchange reaction kinetics of the electrode. Therefore, as expected, the SSC coating significantly enhanced the surface-exchange reaction of LSCF. For a more detailed comparison, the surface-exchange coefficient (k^q) was calculated and analyzed as a function of temperature. Because a dense electrode allows for a clear separation of R_s, the k^q value can be determined from the EIS spectra using the Equation (1):[5,6,37]

$$k^q = \frac{k_B T}{4e^2 ASR c_o} \tag{1}$$

where k_B is the Boltzmann constant, T the absolute temperature, e is the charge of an electron, ASR indicates the area-specific resistance, and c_o represents the total concentration of lattice oxygen. For the SSC materials, k^q was estimated from reported tracer exchange coefficients (k^*) based on the commonly used approximation $k^q \approx k^*$, which is generally applicable to electron-rich mixed ionic-electronic conductors where ionic processes dominate the rate-determining steps.[38,39] As shown in Figure 2b, the temperature dependences of k^q and the corresponding activation energies (E_a) were compared for the SSC/LSCF, LSCF, and SSC electrodes. Our previous study reported the E_a of 1.61 ± 0.09 eV for the oxygen surface-exchange reaction on dense LSCF bulk electrodes,[4] while the known activation energy for SSC is 0.97 eV.[40] As observed in Figure 2b, the activation energy of the SSC/LSCF electrode, fabricated by infiltrating a 0.5 M SSC solution onto a dense LSCF electrode, was measured to be 1.15 eV. This indicates a reduction in E_a and an enhancement in the k^q compared to the LSCF electrode. Solution-based infiltration processes are among the most widely used techniques for forming porous structures via solvent evaporation and precursor pyrolysis.[7–13] Furthermore, considering that the k^q and E_a values of the SSC/LSCF electrode do not fully align with those of the SSC, the infiltrated SSC does not appear to fully govern the oxygen surface-exchange reaction of the LSCF electrode, instead forming a porous layer that acts as a catalyst, thereby facilitating and enhancing the oxygen exchange kinetics on the LSCF electrode. Therefore, forming a porous SSC layer on a dense LSCF electrode provides a suitable model system for analyzing surface-exchange reactions. This strategy is particularly relevant for investigating the effect of the infiltration process on the performance and long-term stability of LSCF electrodes in practical SOFC applications. SSC infiltration was confirmed to effectively enhance the surface-exchange reaction of LSCF, as expected.

2.2. Stability Enhancement of Infiltrated Electrode under SOFC Operating Condition

The stability was examined under biased conditions over an extended period to evaluate its impact on the long-term stability of SOFC. For comparison, both the LSCF electrode and the SSC/LSCF electrode were exposed to an OCV and cathodic conditions (–0.9 V). Because a cathodic bias applies a voltage that drives oxygen into the electrode, it can be considered the operating mode of an SOFC.[6] **Figure 3a** shows the surface-exchange resistance (R_s) of the LSCF and SSC/LSCF electrodes over time at 700 °C. The electrodes were exposed to an OCV for 10 h, followed by a cathodic bias for another 10 h, and then switched back to the OCV. During SOFC operation, both electrodes exhibited a decrease in R_s compared to their initial values under OCV. This reduction is attributed to the increased concentration of oxygen vacancies under cathodic bias, which facilitates the oxygen incorporation reaction, thereby enhancing surface kinetics and lowering the polarization resistance. Meanwhile, owing to the enhanced surface-exchange reaction resulting from SSC deposition, the initial R_s value of the SSC/LSCF electrode was lower than that of the LSCF electrode. However, the more significant difference lies in the degradation behavior: in the case of the LSCF electrode, the application of a cathodic bias followed by a return to OCV conditions resulted in a substantial increase in R_s, indicating severe degradation. In contrast, the SSC/LSCF electrode exhibited minimal degradation even after the application of a cathodic bias, demonstrating significantly improved stability compared to the LSCF electrode. These results indicate that coating the surface with SSC not only enhances the catalytic effect of the LSCF parent electrode but also significantly improves its stability under SOFC operating conditions. As reported in our previous findings, the degradation of the LSCF electrode (ABO_3 perovskite structure) under cathodic bias, i.e., in SOFC operating mode, is primarily attributed to the precipitation of SrO on the surface, along with the simultaneous decomposition of the B-site under cathodic bias.[6] Specifically, LSCF perovskite decomposes into SrO, a spinel phase ($(CoFe)_3O_4$), and a La-rich perovskite in the subsurface region, leading to electrode degradation during SOFC operation.[6] The SEM images presented in Figure 3b illustrate a stark contrast between the LSCF and SSC/LSCF electrodes. The LSCF electrode surface was heavily covered with numerous precipitates, obscuring visibility of the underlying LSCF grains. The significant accumulation of secondary phases on the LSCF surface indicates that these precipitates obstruct the active sites, leading to severe degradation and reduced electrode reactivity. By contrast, the SSC/LSCF electrode exhibited a significantly lower proportion of secondary phases, which were primarily confined to the grain boundaries. Consequently, the SSC/LSCF electrode can be inferred to be exceptionally stable under the SOFC operating conditions, in contrast to the pronounced degradation observed in the LSCF electrode. Under cathodic bias

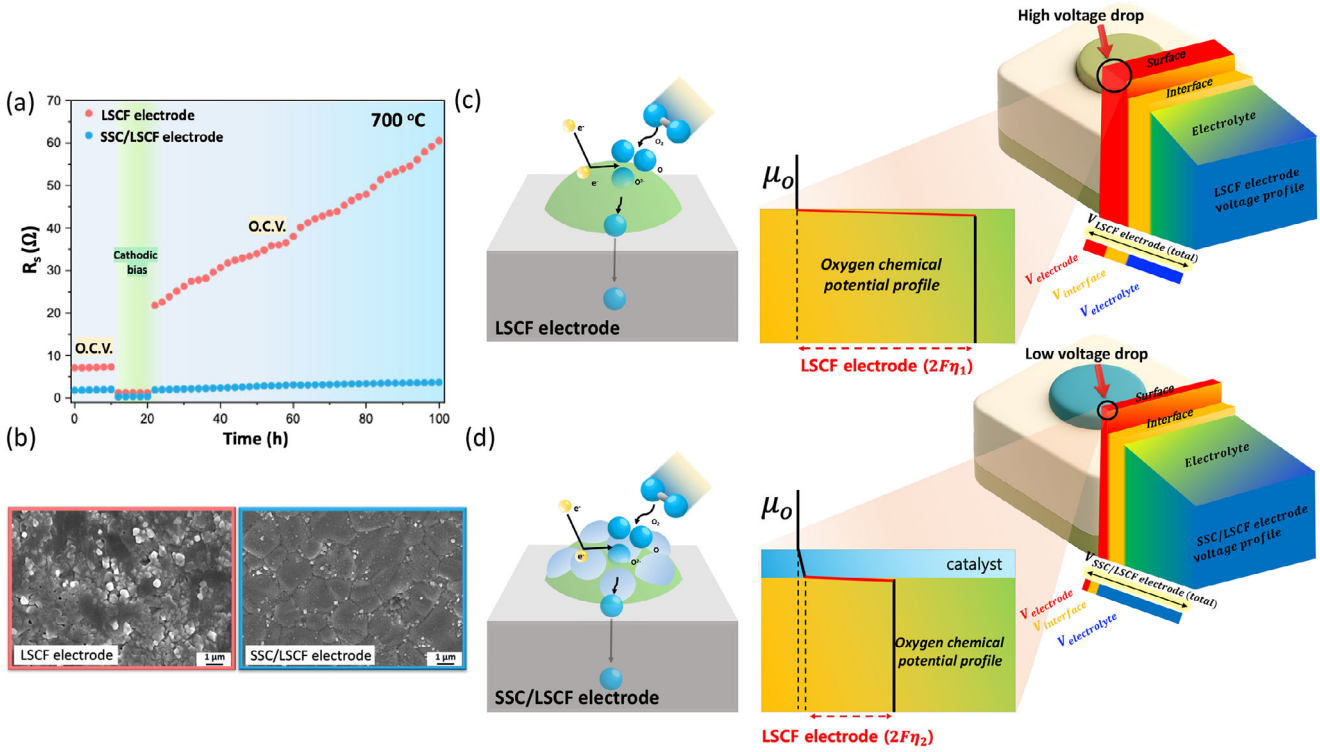

Figure 3. Analysis of deterioration behavior under SOFC operating conditions. a) Time-dependent variation of surface-exchange resistance (R_s) under open-circuit conditions and cathodic bias. Surface SEM image of b) LSCF electrode and SSC/LSCF electrode after impedance spectroscopy. Schematic representation of oxygen-incorporation reaction and voltage profiles for the c) LSCF and d) SSC/LSCF electrodes.

conditions (SOFC operating mode), the electrode is expected to experience a low oxygen partial pressure (P_{O_2}), which corresponds to a relatively reducing environment, as most of the applied potential drops across the surface region rather than being relaxed through bulk transport, due to the surface-exchange reaction being significantly slower than bulk diffusion. Based on our previous study, the phase stability of perovskite electrodes is influenced by the magnitude of the applied bias, which drives cation segregation and phase decomposition in the sub-surface region.[6] Consequently, the observed disparities in the stabilities of the LSCF and SSC/LSCF electrodes can be attributed to the applied bias conditions. Despite applying the same cathodic bias, the SSC/LSCF electrode, in which the surface-exchange reaction was more active, exhibited a relatively lower potential than the LSCF electrode. This indicates that the surface-exchange reaction played a significant role in reducing the effective potential. The Nyquist plots for the LSCF and SSC/LSCF electrodes under a cathodic bias are presented in Figure S2 (Supporting Information) Impedance analysis enabled separation of the R_b and R_i contributions, allowing the effects of the surface-exchange reaction to be independently evaluated. Therefore, the actual potential at the electrode surface was determined. Under a cathodic bias of –0.9 V, impedance analysis reveals that the LSCF electrode experiences a potential of –0.24 V, whereas the SSC/LSCF electrode exhibits a significantly lower potential of –0.11 V. Notably, these values fall within the typical voltage range applied to the cathode during SOFC operation, indicating that the applied potentials are comparable to those under practical SOFC operating conditions. To explain this phenomenon, the oxygen potential profile around the electrode when the electrode reaction is governed by the surface process can be represented as shown in Figure 3c,d. The difference in oxygen chemical potential ($\Delta\mu_O$) across the electrode is given by $2F\eta$, where F denotes the Faraday constant and η represents the overpotential applied across the electrode. As derived from the voltage profile, η_1 (LSCF electrode) > η_2 (SSC/LSCF electrode), indicating that $\Delta\mu_O$ is higher for the LSCF electrode than for the SSC/LSCF electrode. This demonstrates that the catalytic effect of SSC reduces the voltage drop of the LSCF electrode, which inherently enhances the phase stability of the electrode. Furthermore, this confirms that under identical SOFC conditions, SSC enhanced the surface-exchange reaction, reducing the voltage applied to the LSCF electrode. As a result, a relatively low potential is imposed on the electrode surface, improving the phase stability and significantly mitigating issues such as SrO precipitation on the electrode surface.

To gain a deeper understanding of the phase stability-related degradation behavior influenced by the cathodic bias of both the LSCF and SSC/LSCF electrodes, each specimen was analyzed using TEM. **Figure 4** presents a STEM image with EDX mapping, which illustrates the distribution of various elements, specifically La, Sr, Co, Fe, O, and Sm, within both the LSCF and SSC/LSCF electrodes. Both electrodes were subjected to identical electrochemical conditions at 700 °C, as outlined in Figure 3a. These conditions included 10 h of exposure to an OCV, followed by 10 h under cathodic bias, and subsequently returning to the OCV In SOFC mode, the degradation of the perovskite (ABO_3)-structured

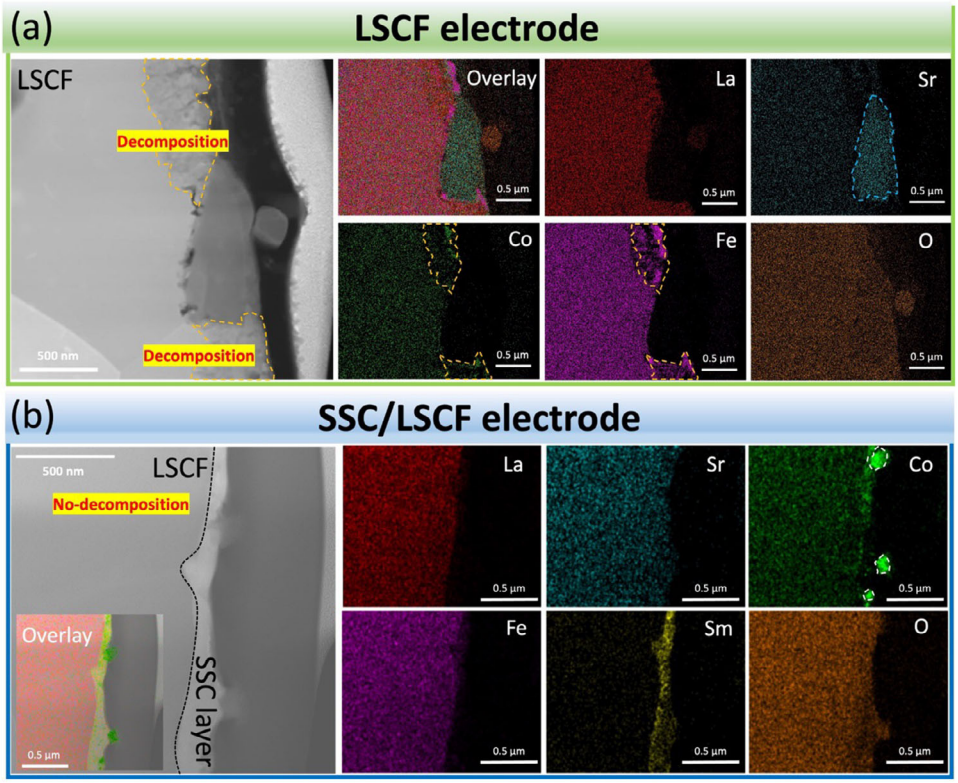

Figure 4. STEM images with EDX mapping of different elements (La, Sr, Co, Fe, O, and Sm) of a) LSCF electrode and b) SSC/LSCF electrode after electrochemical analysis.

LSCF electrode not only leads to the formation of secondary phases, particularly various SrO structures, but also destabilizes the subsurface layer composed of a $(Co,Fe)O_3$ spinel structure.[6] Such decomposition phenomena profoundly hinder the surface-exchange reactions of the electrode. This impairment in surface kinetics ultimately culminates in diminished overall electrochemical performance of the fuel cell. Figure 4a clearly illustrates these features, revealing the presence of secondary phases on the bulk surface of the LSCF electrode, as well as a subsurface layer associated with $(Co, Fe)O_3$, ≈400 nm in depth (Figure S3, Supporting Information). The subsurface region of the LSCF electrode exhibited a distinct morphology compared with that of the inner bulk LSCF. STEM-EDX analysis revealed that this region is mapped with Co, Fe, and O elements. In our previous study, the surface decomposition layer of the LSCF electrode, which had been degraded under similar conditions (600 °C, cathodic bias) for an extended period, was analyzed.[6] STEM-EDX analysis revealed that this region contained Co, Fe, and O. In our previous study, the surface decomposition layer of the LSCF electrode, which was degraded under similar conditions (600 °C, cathodic bias) for an extended period, was analyzed.[6] The STEM-ABF image and fast Fourier-transform pattern matched the crystalline structure of the spinel phase. Based on this finding, the subsurface layer of the LSCF electrode was demonstrated to decompose into a spinel phase associated with B-site elements, while simultaneously forming a La-rich perovskite phase. In this study, we confirmed that a decomposition layer associated with the spinel phase formed on the surface of the LSCF electrode under the same conditions. Although the same cathodic voltage was applied across the entire cell, the air electrode side of the SSC/LSCF electrode exhibited a lower potential (–0.11 V) than that of the LSCF electrode (–0.24 V), indicating an enhanced surface-exchange reaction. Consequently, the degree of reduction for the SSC/LSCF electrode was significantly lower, indicating that it operated under much stable conditions. Therefore, under the same applied voltage, the LSCF electrode was subjected to a stronger cathodic bias, leading to reduced phase stability and thereby facilitating more pronounced SrO precipitation and extensive phase decomposition within the subsurface region, as shown in Figure 4a. By contrast, as shown in Figure 4b and Figure S4 (Supporting Information), although Co-related oxides were observed as surface precipitates on the SSC catalyst layer, the infiltrated SSC layer remained structurally intact atop the LSCF electrode, without evidence of significant phase decomposition or delamination. The slight Co-related precipitation on the SSC surface during SOFC operation can be attributed to elemental interdiffusion, oxygen partial pressure variations, and thermal instability.[41] Notably, in the SSC-coated electrode, the sub-surface region of the LSCF electrode remains intact without decomposition, even after exposure to identical electrochemical conditions. While cobalt oxide-related secondary phases within the SSC layer may lead to a slight increase in the resistance associated with surface-exchange reactions over time, the overall degradation of the LSCF material in the SSC/LSCF electrode remains minimal under an applied cathodic bias. This indicates that the SSC/LSCF configuration maintained its stability under the SOFC operating conditions,

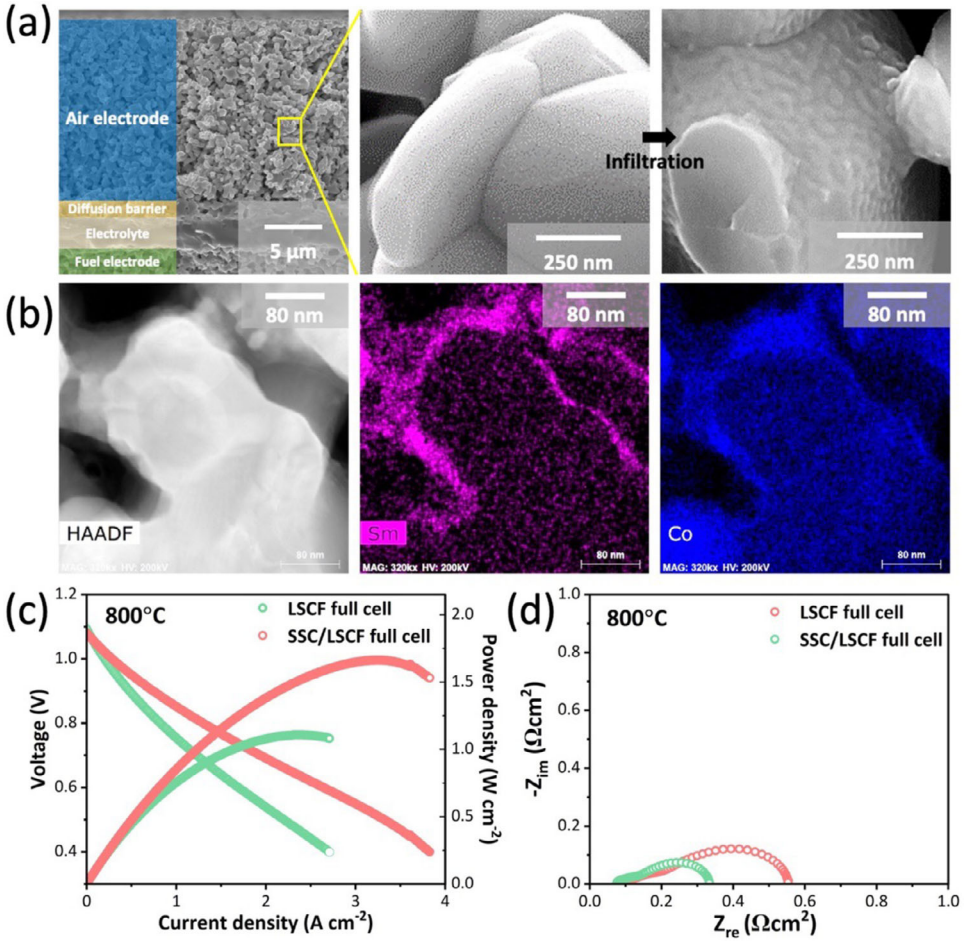

Figure 5. Performance evaluation of full cells. a) SEM images of the full cell and the inner surface of the LSCF cathode before and after SSC infiltration. b) TEM images and EDX maps of Sm and Co for SSC-infiltrated LSCF cathode. c) *I–V* curves and d) Nyquist plots of the LSCF full cell and SSC/LSCF full cell, measured at 800 °C.

which are known to induce instability in conventional electrode materials. SSC infiltration into geometrically well-defined dense bulk LSCF electrodes was confirmed to simultaneously enhance performance and stability.

2.3. Electrochemical Evaluation of Full Cells

To investigate whether this improvement also applies to SOFC cells, performance tests were conducted on SOFC cells with and without the SSC-infiltrated LSCF electrodes. A cross-sectional SEM image of the fabricated cell is shown on the left side of **Figure 5a**. The cell consists of a Ni-YSZ fuel electrode support (≈400 μm), a Ni-YSZ fuel electrode functional layer (≈10 μm), a YSZ electrolyte (≈3 μm), a GDC diffusion barrier (≈2 μm), and an LSCF cathode (≈18 μm). SSC infiltration was performed as described previously.[9,11] The magnified SEM images of the inner surface of the cathode before (LSCF full cell) and after SSC infiltration (SSC/LSCF full cell), shown in the middle and right panels of Figure 5a, were taken from the central region of the porous cathode, as indicated by the yellow square in the left panel. These images demonstrate that the SSC nanocatalysts were uniformly distributed throughout the porous structure, covering a major portion of the LSCF inner surface. The TEM analysis in Figure 5b further confirms the uniform coverage of the LSCF cathode by the SSC nanocatalysts in the SSC/LSCF full cell. Among the constituent elements of SSC, Sm serves as an indicator because it is present only in SSC and not in LSCF. The Sm elemental map clearly shows the uniform distribution of SSC nanocatalysts over the LSCF skeleton. Similarly, Co, which is significantly more abundant in SSC than in LSCF, also shows a strong and uniform signal on the LSCF surface, supporting the uniformity of the SSC nanocatalysts. Generally, infiltration can produce either discrete nanoparticles or a continuous thin film.[10] Discrete nanoparticles are effective in increasing the surface area and enhancing the catalytic properties, whereas thin-film formation may be beneficial in suppressing Sr segregation and improving surface chemical stability. The TEM-EDX image in Figure 5b confirms that the infiltration process successfully formed an SSC layer with a thickness of several tens of nanometers on the surface of the porous LSCF electrode. The overall SSC content is estimated to be less than a few weight percent of the entire electrode, which reasonably suggests that the thermal properties, such as the thermal expansion coefficient, are expected to remain similar to those

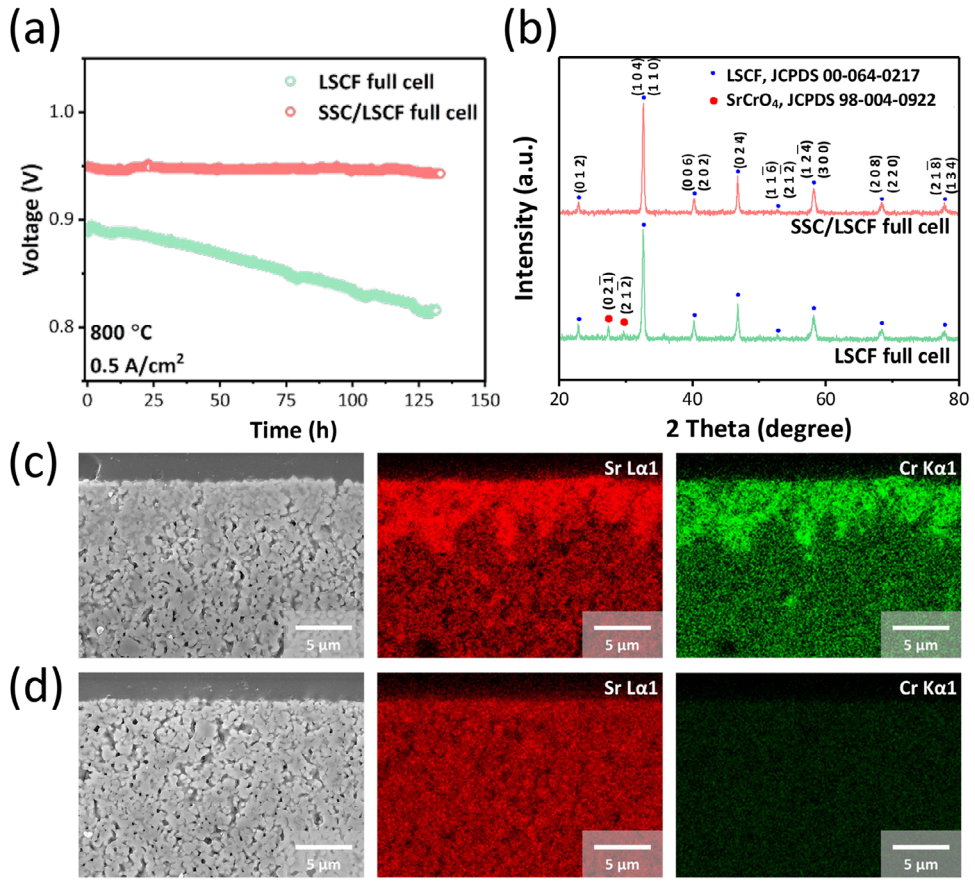

Figure 6. Stability tests and post-mortem analysis. a) Cell voltage as a function of time under constant current of 0.5 A cm^{-2} at 800 °C. b) XRD patterns of the cathode with and without infiltration, collected after long-term tests. c,d) Cross-sectional SEM images and EDX maps of Sr and Cr for the tested cells (c) without and (d) with SSC infiltration.

of the LSCF backbone. This surface modification is expected to contribute to improvements in both the electrochemical performance and long-term stability of the electrode. Subsequently, the performance of the cells with and without SSC infiltration was assessed, and the *I–V* curves of the LSCF full cell and SSC/LSCF full cell at 800 °C are presented in Figure 5c. Both cells exhibited nearly identical OCVs, which were close to the theoretical values, confirming the leakage tightness of the cells or seals. However, the SSC/LSCF full cell achieved a significantly higher maximum power density of 1.7 W cm^{-2} (vs. 1.1 W cm^{-2} for the LSCF full cell) at 800 °C. Figure 5d shows the Nyquist plots of the impedance spectra for the LSCF and SSC/LSCF full cells. In the Nyquist plot, the high-frequency intercept indicates the ohmic resistance, whereas the sum of the resistances corresponding to several arcs represents the polarization resistance. The polarization resistances of the LSCF and SSC/LSCF full cells indicate that the SSC nanocatalysts effectively enhanced the electrode reactions. In addition, the Bode plots of the imaginary parts of the impedance spectra (Figure S5, Supporting Information) exhibit a substantial reduction in impedance within the low-frequency range (1–10 Hz), which corresponds to the surface-exchange reaction of the LSCF electrode.[12,14] The observed decrease in low-frequency impedance confirms that the SSC nanocatalysts primarily enhance the surface-exchange reaction, resulting in improved overall cell performance. Subsequently, the long-term stability of the LSCF full cell and SSC/LSCF full cell was evaluated under a constant current of 0.5 A cm^{-2} at 800 °C. To replicate the real stack-operating conditions, a metallic fixture featuring gas channels and ribs was used, and stability tests were conducted at 800 °C to accelerate degradation, thereby enabling a clearer evaluation of the effect of SSC infiltration. As shown in **Figure 6a**, the SSC/LSCF full cell exhibited a higher initial voltage of 0.95 V (vs. 0.89 V for the LSCF full cell), reflecting the enhanced performance of the SSC/LSCF full cell. Moreover, during the 130 h operation, the LSCF full cell exhibited a rapid voltage drop to 0.8 V, whereas the SSC/LSCF full cell maintained excellent stability with nearly no change over the same period. A comparison of the *I–V* curves (Figure S6, Supporting Information) and impedance spectra (Figure S7, Supporting Information) measured before and after long-term testing confirms that SSC infiltration effectively suppressed degradation. The top surfaces of the cathodes from the tested cells were analyzed using XRD to identify the primary degradation mechanism and to assess the role of SSC infiltration in enhancing the stability, as shown in Figure 6b. In the SSC/LSCF cell, all XRD peaks match the perovskite LSCF phase (JCPDS card no. 00-064-0217), corresponding to a hexagonal structure (space group R-3c), with no secondary phases detected. The absence of distinct SSC peaks

is attributed to its low loading amount of SSC, which is below the detection limit of XRD. In contrast, the LSCF full cell shows additional peaks identified as $SrCrO_4$ (JCPDS card no. 98-004-0922), which adopts a monoclinic crystal system (space group P 1 21/c 1). The cross sections of the tested cells were further analyzed using SEM and EDX, as shown in Figure 6c,d. In the LSCF full cell, pronounced signals for Sr and Cr were identified in the top portion of the LSCF cathode, whereas the SSC/LSCF full cell exhibited uniform Sr distribution throughout the cathode and a significantly weaker Cr signal. To further investigate the degradation phenomena in the LSCF full cell, additional X-ray photoelectron spectroscopy (XPS) analyses were performed, as shown in Figures S8 and S9 (Supporting Information). The Sr 3d spectra were deconvoluted into lattice and surface components, revealing that the surface-associated Sr fraction increased substantially from 0.58 in the as-prepared state to 0.83 after long-term testing.[42] This increase indicates significant Sr migration and segregation to the surface, leading to the formation of Sr-rich phases such as SrO or $SrCrO_4$ that can block active sites and degrade ORR performance. Additionally, the Cr 2p spectra were fitted to reveal substantial contributions from both Cr^{6+} and Cr^{3+} species, consistent with the presence of $SrCrO_4$ and Cr_2O_3 phases.[43] These observations confirm that degradation in the LSCF full cell involves Sr and Cr migration and the formation of insulating secondary phases at the cathode surface, consistent with the formation of $SrCrO_4$ observed in the XRD analysis. Additional SEM-EDX maps of the constituent elements are presented in Figure S10 (Supporting Information). In the LSCF full cell, local Co and Fe segregation is observed, whereas the SSC/LSCF full cell exhibits only minor Co segregation. These elemental distribution trends are consistent with those observed in the corresponding dense electrodes shown in Figure 4. This analysis indicates that Cr poisoning is the primary degradation mechanism. A metallic interconnect without a protective coating results in significant Cr evaporation during high-temperature operations. The Cr vapor readily reacts with Sr in the LSCF cathode, forming a Sr- and Cr-containing insulating oxide layer on the top surface of the cathode, which deteriorates cell performance.[44–51] According to various studies, the Cr-poisoning phenomenon is accelerated under conditions of high current density and polarization, leading to the deterioration of cathode kinetics.[46,47] In the case of the LSCF full cell, Cr poisoning is primarily driven by the interaction between SrO precipitated on the electrode surface and volatile chromium species released from the interconnect, resulting in the formation of significant $SrCrO_4$ deposits, as shown in the XRD patterns (Figure 6b). In this study, the LSCF full cell without SSC was exposed to a higher current potential than the SSC/LSCF full cell, which accelerated the precipitation of SrO and consequently promoted the formation of $SrCrO_4$. This indicates that the extent of Cr poisoning is strongly correlated with the electrochemical conditions that influence SrO segregation. In electrochemical analysis, a higher resistance in a specific component signifies a greater voltage drop within that component from the applied voltage. The difference in cell configuration between the SSC/LSCF full cell and the LSCF cell lies in the presence or absence of infiltrated SSC materials on the surface of the LSCF cathode. Thus, the resistance differences between the two cells arise solely from surface-exchange reactions on the LSCF cathode side rather than from reactions occurring in the electrolyte or on the anode side. Therefore, in the case of the SSC/LSCF full cell, the enhanced activity of the surface-exchange reaction on LSCF resulted in a reduced voltage drop across LSCF. Consequently, the phase stability relatively improved, significantly suppressing the precipitation of SrO and the formation of $SrCrO_4$. As a result, not only was the performance improved, but long-term stability was also significantly enhanced. Our experiments demonstrate that the kinetic activation of the LSCF electrode reaction through infiltration significantly reduces the polarization applied to the electrode, thereby enhancing the phase stability of LSCF—even during actual SOFC operation—while simultaneously improving the overall performance of the SOFC. Infiltration into geometrically well-defined dense bulk electrodes simultaneously enhanced performance and stability, and this result was consistently observed in actual SOFC cells. This finding provides crucial evidence that the infiltration method can simultaneously improve performance and operational stability, clarifying the underlying mechanism.

3. Conclusion

This study elucidated the critical role of SSC surface coatings in enhancing both the performance and stability of LSCF electrodes in SOFC by systematically investigating their effects on both dense model electrodes and practical full-cell systems. The use of dense bulk electrodes allowed us to isolate and quantify intrinsic surface-exchange properties without the geometric complexities of porous structures, enabling direct analysis of local oxygen chemical potential gradients and associated degradation behavior. The results demonstrate that the introduction of SSC as a catalyst not only enhances the surface-exchange kinetics but also substantially improves the stability of the electrode system under polarization-induced operational conditions. In densely modeled LSCF electrodes, the catalytic effect of the SSC enhances the surface-exchange reaction, thereby reducing the voltage drop of the LSCF backbone and inherently improving its phase stability. Consequently, phase decomposition, including the precipitation of SrO, was effectively suppressed, leading to significantly improved long-term stability. Furthermore, consistent results were observed in an actual SOFC connected with metallic interconnectors, demonstrating simultaneous improvements in performance and stability. The infiltrated SSC layer enhances the stability of the oxygen reduction reaction by effectively mitigating the formation of Sr-related precipitates, such as SrO and $SrCrO_4$, as well as suppressing the phase decomposition of the electrode, which are known to block active sites and deteriorate performance. This enhanced stability resulting from SSC infiltration can be attributed to a reduction in the polarization effect on the LSCF electrode, indicating that the active coating layer plays a critical role in mitigating the decomposition of the backbone material. Overall, this study provides new mechanistic insight into the relationship between infiltration, electrode potential, and degradation suppression, offering a deeper understanding of how infiltrated catalysts can enhance the operational lifespan and reliability of SOFC electrodes. These findings are expected to guide the development of strategic approaches to improve the performance and stability of future electrochemical cells.

4. Experimental Section

Preparation of Chemical Solutions: A precursor solution for SSC infiltration was formulated by dissolving stoichiometric ratios of $Sm(NO_3)_3$ $6H_2O$, $Sr(NO_3)_2$, and $Co(NO_3)_2$ $6H_2O$ (98%, Sigma–Aldrich, USA), in a 1:1 mixture of deionized water and ethanol. Urea (99%, Sigma–Aldrich, USA) and glycine (99%, Daejung, Korea) were introduced as chelating agents at urea-to-cation and glycine-to-cation molar ratios of 10 and 1, respectively. All chemicals were used as received without further purification. The resulting solution was dried at 80 °C for 1 h and subsequently calcined at 650 °C for 1 h to obtain the SSC powder. The crystalline phase was confirmed by X-ray diffraction (XRD; Rigaku D/max-2500, Japan), as shown in Figure S1 (Supporting Information).

EIS (Electrochemical Impedance Spectroscopy) Characterization: The $La_{0.6}Sr_{0.4}Co_{0.2}Fe_{0.8}O_{3-\delta}$ (LSCF) dense bulk electrode was fabricated using a ceramic process. Initially, a slurry was prepared by mixing LSCF and $Gd_{0.1}Ce_{0.9}O_{1.95}$ (GDC) powders (K-Ceracell, Republic of Korea) in a solution. To lower the sintering temperature for the GDC electrolyte, 1 vol% LSCF was blended into the GDC electrolyte powder as a sintering aid. Ethanol and n-propyl acetate were used as solvents for the slurry, which was combined with a dispersant (BYK-103), dioctyl phthalate, and polyvinyl butyral (PVB-76) to create a homogeneous solution. The resulting mixture, containing 50 wt.% solid and 50 wt.% liquid was thoroughly mixed for 48 h using a ball mill. This slurry was then tape-cast into film sheets and subsequently dried to produce a green tape. Upon completion of the tape-casting process, the GDC electrolyte was formed by laminating 20 layers of green tape under 43 MPa at 70 °C using warm isostatic pressing (WIP). The green tapes for both the electrode and electrolyte were then shaped into round (10 mm diameter) and square (15 mm length) shapes using a laser-cutting system (Laser Tools and Technics Corp., Taiwan, ILS-3 NM 55 W). The LSCF green sheet was centered on the GDC electrolyte and laminated at 70 °C under a pressure of 43 MPa using WIP. After co-sintering at 1300 °C for 4 h, the LSCF electrode and GDC electrolyte were densified. A porous LSCF counter electrode was deposited on the opposite side of the dense electrode by brush-printing and subsequently annealed at 1000 °C for 3 h. After the annealing process, the electrode surface was treated with 9 mol L^{-1} aqueous hydrochloric acid for 5 s to eliminate surface impurities. Subsequently, a platinum paste (Heraeus, #6082, Germany) was spread over ≈20% of the total surface area of the dense electrode, and a platinum mesh was then attached to the pasted area on both sides before annealing at 800 °C for 1 h. The fabricated bulk electrodes were electrochemically characterized with a 10 mV perturbation over a frequency range from 1 MHz to 5 mHz, applying six points per frequency decade. The lamellae were prepared using a dual-beam focused ion beam system (Helios NanoLab, FEI, USA). Microstructural and elemental analyses were carried out via ultrahigh-resolution field-emission scanning electron microscopy (Thermo Fisher Scientific, Verios 5UC, USA) and transmission electron microscopy (TEM; FEI Company, Tecnai G2 F30 S-Twin, USA). Elemental distribution across the electrode surface was analyzed via energy-dispersive X-ray spectroscopy (EDX) operated in scanning transmission electron microscopy (STEM) mode.

Construction and Electrochemical Evaluation of Full Cells: Full cells were fabricated using a commercial substrate (Elcogen, Estonia), which includes a ≈400 µm Ni-YSZ anode support, a ≈10 µm Ni-YSZ functional layer, a ≈3 µm YSZ electrolyte, and a ≈2 µm GDC barrier layer. The cathode paste was prepared by mixing LSCF powder (Kceracell, Korea) with dispersant (Hypermer KD-6, Croda Inc, USA), binder (BH-3, Sekisui chemical, Japan), plasticizer (dibutyl phthalate, Junsei, Japan), and solvent (α-terpineol, Kanto chemical, Japan) in a planetary mill. The paste was applied over the GDC diffusion barrier layer by screen printing, covering an active electrode area of 1 cm^2, and was subsequently sintered at 1050 °C for 3 h. SSC infiltration was performed by dropwise injecting 2 µL of a 0.5 M SSC solution onto the surface of the LSCF air electrode (area: 1 cm^2, thickness: 18 µm) using a micropipette, followed by heat treatment at 80 °C for 1 h and then at 650 °C for 1 h. This entire process was repeated for two cycles, allowing precise control over the total precursor loading and thus the coating thickness, while minimizing the risk of local aggregation or uneven coverage. The microstructures of the fabricated cells were characterized using scanning electron microscopy (SEM; Regulus 8230, Hitachi) and TEM (F200X, Talos). For the electrochemical characterization, the cell was assembled between Inconel testing fixtures and sealed with glass–ceramic sealant. Ni foam and a Pt mesh served as current collectors for the anode and cathode, respectively. The assembly was heated to 800 °C in an electric furnace with humidified H_2 (3% H_2O) and air supplied to the anode and cathode, respectively, at a flow rate of 300 sccm. Electrochemical measurements were conducted using a Solartron 1260/1287 frequency response analyzer and a potentiostat. Long-term stability tests were carried out at a constant current density of 0.5 A cm^{-2} at 800 °C. The chemical states of Sr 3d and Cr 2p in the LSCF full cell were analyzed by X-ray photoelectron spectroscopy (XPS; Nexsa, Thermo Fisher Scientific).

Supporting Information

Supporting Information is available from the Wiley Online Library or from the author.

Acknowledgements

This work was supported by the New and Renewable Energy Core Technology Development of the Korea Institute of Energy Technology Evaluation and Planning (KETEP) granted financial resource from the Ministry of Trade, Industry & Energy (20223030040040). This research also was supported by the program of H2 Next Round through the National Research Foundation of Korea (NRF) funded by the Ministry of Science and ICT (RS-2024-00467191). This work also was supported by the Technology Innovation Program (RS-2024-00432125, Development of Evaluation and Electrochemical Diagnostics Technology for Advanced K-SOEC Stack) funded by the Ministry of Trade, Industry & Energy (MOTIE, Korea). This work was also funded by the Korea Institute of Science and Technology (KIST) Institutional Program (2E32570 and 2E32574).

Conflict of Interest

The authors declare no conflict of interest.

Author Contributions

J.L. and J.P. contributed equally to this work. J.L., J.P. and T.K. prepared the samples and electrochemical measurements. J.L. and J.P. analyzed the electrochemical data. T.K., S.C. and S.K. provided feedback and refined the manuscript. All the authors discussed the results and contributed to the writing of the manuscript. K.J.Y. and J.H.J. designed and supervised this study.

Data Availability Statement

The data that support the findings of this study are available from the corresponding author upon reasonable request.

Keywords

infiltration, solid oxide electrochemical cell, stability enhancement, surface modification, surface potential

Received: June 2, 2025
Revised: July 2, 2025
Published online: August 14, 2025

[1] E. Wachsman, T. Ishihara, J. Kilner, *MRS Bull.* **2014**, *39*, 773.
[2] J. Ralph, A. Schoeler, M. Krumpelt, *J. Mater. Sci.* **2001**, *36*, 1161.
[3] M. T. Mehran, M. Z. Khan, R.-H. Song, T.-H. Lim, M. Naqvi, R. Raza, B. Zhu, M. B. Hanif, *Appl. Energy* **2023**, *352*, 121864.
[4] J. Lee, M. Kim, Y. Lee, J. H. Joo, *Chem. Mater.* **2021**, *33*, 6290.
[5] J. Lee, T. Kim, H. J. Lee, K. J. Yoon, J.-H. Lee, J. H. Joo, *Chem. Eng. J.* **2025**, *505*, 159654.
[6] J. Lee, Y. Shin, T. Kim, W. Choi, M.-H. Jung, Y.-M. Kim, K. J. Yoon, H. Y. Jeong, D. Lee, J. H. Joo, *Chem. Mater.* **2024**, *36*, 2933.
[7] H. Cho, H. Seo, J. Min, J.-e. Won, J. Hong, K. J. Yoon, *J. Mater. Chem. A* **2024**, *12*, 28002.
[8] S. S. Shin, J. H. Kim, H. Jeong, M. Y. Park, K. J. Yoon, J.-W. Son, M. Choi, H. Kim, *Nano Lett.* **2021**, *21*, 10186.
[9] M. Y. Park, J. Shin, S.-Y. Park, J.-e. Won, J. Y. Hwang, S. Hong, S.-W. Kim, J.-H. Jang, K. J. Yoon, *Chem. Eng. J.* **2023**, *476*, 146924.
[10] D. Ding, X. Li, S. Y. Lai, K. Gerdes, M. Liu, *Energy Environ. Sci.* **2014**, *7*, 552.
[11] K. J. Yoon, M. Biswas, H.-J. Kim, M. Park, J. Hong, H. Kim, J.-W. Son, J.-H. Lee, B.-K. Kim, H.-W. Lee, *Nano Energy* **2017**, *36*, 9.
[12] S.-i. Lee, J. Kim, J.-W. Son, J.-H. Lee, B.-K. Kim, H.-J. Je, H.-W. Lee, H. Song, K. J. Yoon, *J. Power Sources* **2014**, *250*, 15.
[13] X. Lou, S. Wang, Z. Liu, L. Yang, M. Liu, *Solid State Ion.* **2009**, *180*, 1285.
[14] J. Kim, D. Shin, J.-W. Son, J.-H. Lee, B.-K. Kim, H.-J. Je, H.-W. Lee, K. J. Yoon, *J. Power Sources* **2013**, *241*, 440.
[15] G.-J. Yang, C.-J. Li, C.-X. Li, K. Kondoh, A. Ohmori, *J. Therm. Spray Technol.* **2013**, *22*, 36.
[16] Y. Namgung, A. Kumar, J. Hong, I.-H. Kim, S.-J. Song, *J. Alloys Compd.* **2021**, *852*, 157037.
[17] P. Wu, Y. Tian, Z. Lü, X. Zhang, L. Ding, *Int. J. Hydrog.* **2022**, *47*, 747.
[18] Y.-H. Song, S. U. Rehman, H.-S. Kim, H.-S. Song, R.-H. Song, T.-H. Lim, J.-E. Hong, S.-J. Park, J.-Y. Huh, S.-B. Lee, *J. Mater. Chem. A* **2020**, *8*, 3967.
[19] L. Zhao, G. Li, K. Chen, Y. Ling, Y. Cui, L. Gui, B. He, *J. Power Sources* **2016**, *333*, 24.
[20] Z. Song, H. Pan, G. Wan, A. Wu, Q. Chen, W. Guan, S. C. Singhal, *Int. J. Hydrog.* **2023**, *48*, 27095.
[21] B.-K. Park, D. Cox, S. A. Barnett, *Nano Lett.* **2021**, *21*, 8363.
[22] M. Zhi, S. Lee, N. Miller, N. H. Menzler, N. Wu, *Energy Environ. Sci.* **2012**, *5*, 7066.
[23] S. Ovtar, X. Tong, J. J. Bentzen, K. T. Thydén, S. B. Simonsen, M. Chen, *Nanoscale* **2019**, *11*, 4394.
[24] T. L. Skafte, J. Hjelm, P. Blennow, C. Graves, *J. Power Sources* **2018**, *378*, 685.
[25] L. Spiridigliozzi, E. Di Bartolomeo, G. Dell'Agli, F. Zurlo, *Appl. Sci.* **2020**, *10*, 3882.
[26] J. Grimes, J. Hong, S. A. Barnett, *J. Power Sources* **2022**, *551*, 232189.
[27] E. Filonova, E. Pikalova, *Materials* **2023**, *16*, 4967.
[28] M. Y. Lu, T. Yang, R. Scipioni, Y. A. Chart, A. Furlong, S. A. Barnett, *J. Electrochem. Soc.* **2020**, *167*, 164504.
[29] L. da Conceição, A. M. Silva, N. F. Ribeiro, M. M. Souza, *Mater. Res. Bull.* **2011**, *46*, 308.
[30] V. Vibhu, S. Yildiz, I. C. Vinke, R.-A. Eichel, J.-M. Bassat, L. De Haart, *J. Electrochem. Soc.* **2019**, *166*, F102.
[31] L. Agun, H. A. Rahman, S. Ahmad, A. Muchtar, *Adv. Mat. Res.* **2014**, *893*, 732.
[32] H. Wang, W. Zhang, K. Guan, Z. Wei, J. Meng, J. Meng, X. Liu, *ACS Sustainable Chem. Eng.* **2020**, *8*, 3367.
[33] H. Chen, Z. Guo, L. A. Zhang, Y. Li, F. Li, Y. Zhang, Y. Chen, X. Wang, B. Yu, J.-m. Shi, *ACS Appl. Mater. Interfaces.* **2018**, *10*, 39785.
[34] F. S. Baumann, J. Fleig, H.-U. Habermeier, J. Maier, *Solid State Ion.* **2006**, *177*, 1071.
[35] G. M. Rupp, A. K. Opitz, A. Nenning, A. Limbeck, J. Fleig, *Nat. Mater.* **2017**, *16*, 640.
[36] B. Steele, *Solid State Ion.* **1995**, *75*, 157.
[37] N. Simrick, A. Bieberle-Hütter, T. Ryll, J. Kilner, A. Atkinson, J. Rupp, *Solid State Ion.* **2012**, *206*, 7.
[38] R. Merkle, J. Maier, J. Fleig, *Handbook of fuel cells* **2010**.
[39] J. Maier, *Solid State Ionics* **2000**, *135*, 575.
[40] S.-L. Zhang, H. Wang, M. Y. Lu, A.-P. Zhang, L. V. Mogni, Q. Liu, C.-X. Li, C.-J. Li, S. A. Barnett, *Energy Environ. Sci.* **2018**, *11*, 1870.
[41] R. Scurtu, S. Somacescu, J. M. Calderon-Moreno, D. Culita, I. Bulimestru, N. Popa, A. Gulea, P. Osiceanu, *J. Solid State Chem.* **2014**, *210*, 53.
[42] Z. Shen, J. M. Bassat, S. Fourcade, A. Demourgues, E. Durand, L. Teule-Gay, M. Duttine, J. Gamon, *Adv. Energy Mater.* **2024**, *14*, 2401518.
[43] J. Sun, S. T. Wang, L. Tong, J. Wang, S. A. Suhaib, Y. M. Xie, G. B. Zhu, C. C. Wang, *J. Alloys Compd.* **2018**, *764*, 300.
[44] C. Harrison, P. Slater, R. Steinberger-Wilckens, *Solid State Ion.* **2020**, *354*, 115410.
[45] X. Chen, *Int. J. Hydrog.* **2014**, *39*, 505.
[46] R. Wang, U. B. Pal, S. Gopalan, S. N. Basu, *J. Electrochem. Soc.* **2017**, *164*, F740.
[47] N. Ni, C. C. Wang, S. J. Skinner, *J. Mater. Chem. A* **2019**, *7*, 9253.
[48] C. Xiong, P. Qiu, W. Zhang, J. Pu, *Ceram. Int.* **2022**, *48*, 33999.
[49] J. Huang, Q. Liu, L. Zhao, N. Ai, X. Wang, Y. Shao, C. Guan, H. Fang, Y. Luo, K. Chen, *Appl. Catal. B.* **2023**, *321*, 122080.
[50] H. A. Ishfaq, M. Z. Khan, Y. M. Shirke, S. Qamar, A. Hussain, M. T. Mehran, R.-H. Song, M. Saleem, *Appl. Catal. B.* **2023**, *323*, 122178.
[51] H. G. Seo, H. Kim, W. Jung, H. L. Tuller, *Appl. Catal. B.* **2024**, *355*, 124172.